energy&fuels

Article

Cite This: Energy Fuels 2017, 31, 13317−13328

pubs.acs.org/EF

Quantitative Analysis of Nanopore Structural Characteristics of Lower Paleozoic Shale, Chongqing (Southwestern China): Combining FIB-SEM and NMR Cryoporometry

Shaoqing Tong,[†,‡,⊥] Yanhui Dong,*[,†,⊥,‡,§] Qian Zhang,[†,‡,⊥] Derek Elsworth,[§] and Shimin Liu[§]

[†]Key Laboratory of Shale Gas and Geoengineering, Institute of Geology and Geophysics, Chinese Academy of Sciences, Beijing 100029, China

[‡]University of Chinese Academy of Sciences, Beijing 100049, China

[⊥]Institutions of Earth Science, Chinese Academy of Sciences, Beijing 100029, China

[§]Department of Energy and Mineral Engineering, G3 Center and EMS Energy Institute, The Pennsylvania State University, University Park, Pennsylvania 16802, United States

ABSTRACT: Characterizing nanopore structure is one of the most important factors in understanding gas storage and transport in shale reservoirs, but remains a significant challenge. In this work, we combine the benefits of Focused Ion Beam Scanning Electron Microscopy (FIB-SEM) and Nuclear Magnetic Resonance Cryoporometry (NMR-C) to characterize the nanopore structure of lower Paleozoic shales from Chongqing, southwestern China. Mineral composition is qualified through X-ray Energy Dispersive Spectroscopy (EDS) and Field-Emission Scanning Electron Microscopy (FE-SEM). Voids in 2D micrographs are classified into types of meso- and/or microfractures, inter particle pores (InterP pores), intraparticle pores (IntraP pores), and pores in organic matter (OM pores). An Otsu thresholding algorithm and an edge detection algorithm (in Avizo) are used to segment OM, InterP, and IntraP pores and to establish 3D pore structure for pore-network modeling (PNM). The pore size distribution (PSD) is measured via PNM and compared to the PSD recovered from NMR-C. Results indicate that the small OM pores have favorable potential for storing adsorbed gas because of their apparent interconnectivity and higher porosity; conversely, InterP and IntraP pores are mostly isolated and with low porosity. The peaks of the PSD, recovered from PNM, are in the ranges 10−20 nm and 60−120 nm and are in good agreement with the peaks of the PSD recovered from NMR-C. This suggests that the NMR signals in these discontinuous ranges are due to OM, InterP, and IntraP pores. This indirectly demonstrates that the probe liquid in the NMR-C experiments (i.e., water) may indeed enter the nanoscale pores in the shale during centrifugal saturation. Comparison of the PSD from PNM and NMR-C also shows that NMR-C has a higher sensitivity and accuracy in detecting nanopores. Combining FIB-SEM and NMR-C is a promising technique in detecting and characterizing the nanoporosity of shales.

1. INTRODUCTION

Shale gas is an important energy resource with rapid development in North America.[1,2] It is expected to play an increasingly important role in Asia and Europe in the near future.[3] In recent years, the lower Paleozoic shale gas reservoirs in the Sichuan Basin, southwestern China have been explored and developed.[4,5] The Weiyuan 201 Well (W201) was the first in China to provide industrial-scale gas flow after hydraulic fracturing. The thermal maturity of the organic matter of the ancient shales in the Sichuan Basin is higher than that of the Barnett, Marcellus, and Haynesville formations in North America, implying a lower degree of development of the pores in the organic matter.[6] Previous studies have indicated that shale pore structure has a strong influence in controlling the shale gas content and storage and transport mechanisms.[7−9] In particular, pores in organic matter provide the main storage space for absorbed gas in shale.[10,11,2,12] Hence, a correct understanding of the 2D and 3D pore structure is the foundation for shale gas exploration, development, and research.[9,13]

As a typical low permeability reservoir, shale is a fine-grained, compact sedimentary rock comprising pores and fractures at a variety of scales. The 2D and 3D pore morphology, size distribution, and other features of shale have been investigated by many imaging methods. These include field-emission scanning electron microscopy (FE-SEM), FE-SEM coupled with focused gallium ion beam (FIB-SEM), or Nano X-ray computed tomography (Nano-XCT).[2,5,14−16] Four scales of void space can be identified in shale reservoirs. These include mesoscale fractures, meso- and/or microfractures, interparticle and intraparticle pores (InterP pores and IntraP pores), and nanoscale pores in organic matter (OM pores).[2,3,14,17,18] Imaging methods are able to distinguish different types of pores in shale. Nano-XCT is a nondestructive method using transmission X-ray attenuation imaging and is widely applied to detect pores in shales. Nano-XCT has been used to study the development of nanopores in the Chang 7 Member of organic-rich shale[19] and to characterize the connection of typical 3D pores in the Jiulaodong formation.[2] However, the minimum voxel size for Nano-XCT is approximately 32−50 nm, limiting

Received: August 15, 2017
Revised: November 30, 2017
Published: November 30, 2017

DOI: 10.1021/acs.energyfuels.7b02391
Energy Fuels 2017, 31, 13317−13328

the resolution of pores that must transit of the order of three voxels.

FIB-SEM usually provides 3D micrographs at fine spatial resolutions of ~10 nm.[20,21] Although milling and imaging layer-by-layer can partly damage the shale sample, nanopores in FIB-SEM micrographs are much more distinguishable than those recovered by Nano-XCT. However, previous studies[3,11,14] show that the majority of pores in organic matter range from 2 nm to tens of nanometers. A few could be as large as a few hundred nanometers. This means that FIB-SEM could not cover the entire pore size distribution (PSD). In addition, FIB-SEM has a small field of view.

Nuclear magnetic resonance cryoporometry (NMR-C) is a novel and emerging technique that can probe PSD from 2 nm to several micrometers, generally more than 3 orders of magnitude. It is based upon the pore-diameter-related melting and/or freezing points of pore imbibed materials.[11,12,22−24] For detection, NMR-C exploits the transverse relaxation time difference between solid and liquid NMR signals.[22] Firouzi et al.[22] first reported PSD measurement using NMR-C method on shale, but they failed because the NMR instrumentation used could not scan temperatures lower than 253 K to detect pores with size smaller than 6 nm. Using improved NMR instrumentation and saturation methods, later research[11,23,24] successfully measured the PSD of shale using NMR-C. Fleury et al.[23] compared the PSDs from NMR relaxation and NMR-C in shales and found that the PSD obtained from cryoporometry is quasi uniform from 2 nm up to 100 nm. Zhang et al.[24] utilized NMR-C to examine both bulk matrix and pulverized shale samples with the results surprisingly indicating that the porosity of the bulk sample was apparently smaller than that of the pulverized shale sample. Li et al.[25] used NMR-C, NMR, mercury intrusion porosimetry, and gas adsorption methods to study pore structure characteristics of shales in Southwestern China. They obtained good agreement in the PSDs between the various methods. All previous studies focused on the applicability and accuracy of NMR-C compared with other intrusive methods when probing pore structures in shale. However, comparisons of NMR-C with imaging methods have been rarely reported.

In this work we use both FIB-SEM and NMR-C to characterize the nanopore structure of shale. 3D pore structure modeling and pore network modeling (PNM) are used for the analysis of OM pores as well as InterP and IntraP pores in shale from the W201 well. Additionally, the PSDs obtained from PNM and NMR-C are quantitatively analyzed and contrasted to understand and assess the corresponding types and structure of nanoporosity in shale.

2. GEOLOGICAL SETTING

The shale samples were taken from the Weiyuan area in western Chongqing, from the upper Yangtze Platform. The Weiyuan area extends over about 2700 km^2 in the southwestern part of the Sichuan Basin (Figure 1). The region is bordered on the southeastern edge of the Leshan-Longnvsi paleo-uplift and is characterized as a large-scale NEE-SEW oriented domal anticline.[26] The Weiyuan area has experienced three major orogenies, comprising the Caledonian, Indosinian, and Himalayan. Emergent Proterozoic and Paleozoic strata in this area are mainly from the Sinian, Cambrian, Ordovician, Silurian, and Permain periods (Figure 2).

The upper Sinian is subdivided into the Dengying and Doushantuo formations with a total thickness of 659−670 m.[26,27] The Dengying formation comprises mainly micro-crystalline dolomite and is the main conventional gas reservoir in the Weiyuan area.[27,28] A total of 766−1019 m of the Cambrian unit consists of the Jiulaodong and Yuxiansi formations in the lower Cambrian and the Xixiangchi formation in the upper Cambrian.[29,30] The Jiulaodong formation contains two-thirds of the sedimentary column of organic-rich black shales with a thickness of 230−400 m. It is uniformly distributed in the Weiyuan area and is the dominant source rock and caprock of the Sinian gas reservoir. It is also the target

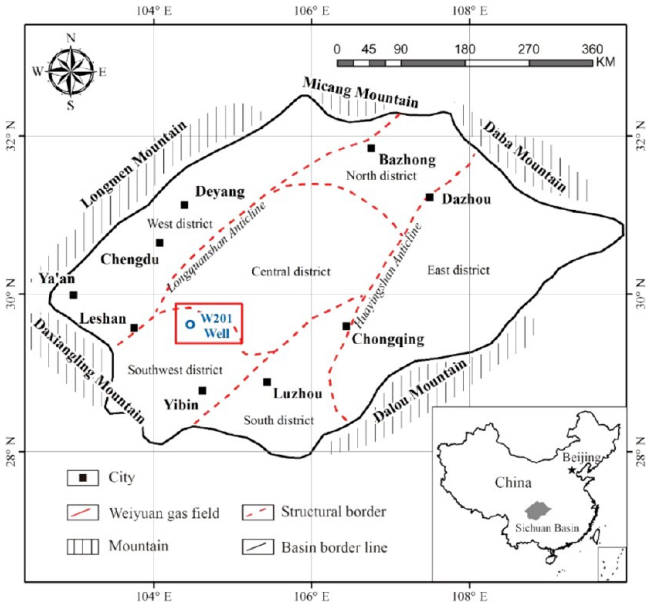

Figure 1. Schematic illustrating the primary structural outline and border of the Sichuan Basin, the location of the Weiyuan gas field and the W201 well, relative to major cities.

System	Series	Formation	Lithology	Thickness (m)
Permian	Upper	Longtan	Limeston、shale	182~242
	Lower	Maokou	Limeston	204~459
Silurian	Lower	Longmaxi	shale	0~140
Ordovician	Middle	Baota	shale、Limeston	51~75
	Lower	Dachengsi	Dolomite	131~280
		Luohanpo		
Cambrian	Mid Upper	Xixiangchi	Sandstone、Dolomite	145~259
	Lower	Yuxiansi	Sandstone、Dolomite	212~246
		Jiulaodong	shale	230~400
Sinian	Upper	Dengying	Dolomite	648~654
		Doushantuo	Dolomite	11~16

Figure 2. Stratigraphic column of the Weiyuan area including chronology, lithology, and thickness. The gray denotes shale gas source formations in southwestern China.

DOI: 10.1021/acs.energyfuels.7b02391
Energy Fuels 2017, 31, 13317−13328

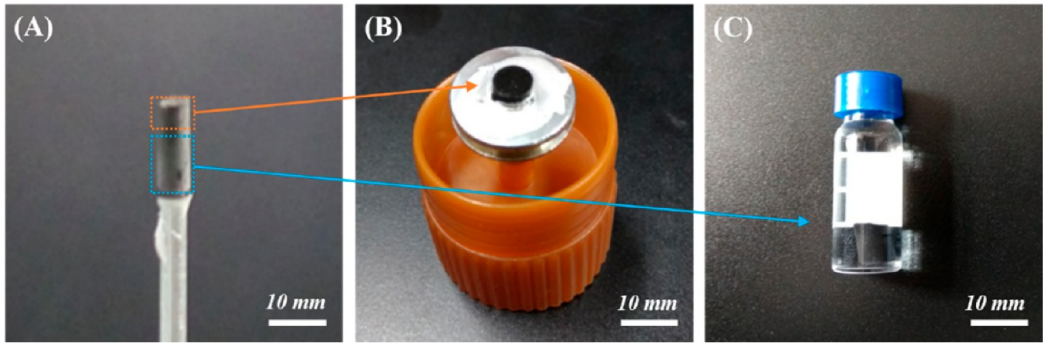

Figure 3. Sample preparation details. (A) 4 mm diameter cylindrical shale samples recovered by core drill. A third of the sample (orange box) is used for FE-SEM and FIB-SEM with the other two-thirds (blue box) used for NMR-C. (B) Argon ion polished samples for FE-SEM and FIB-SEM, sheathed in a silver conductive adhesive. (C) Shale sample in the NMR-C sample tube with ultrapure water.

formation of the W201 well.[29] The Yuxiansi and Xixiangchi formations are primarily interbedded with sandstone and siltstone. The Ordovician strata are poorly developed in the Weiyuan area due to the advent of the Caledonian orogeny. The lower Ordovician Luohanpo and Dachengsi formations are dominated by dolomite with a total thickness of 131−280 m, while the middle Ordovician Baota formation mainly consists of limestone with thick shales.

The lower Silurian Longmaxi formation is a set of organic-rich sedimentary black shales and silty mudstones in southeastern Weiyuan, but is absent in the northwestern part of this region. The Longmaxi formation is an important shale gas source in southwestern China. However, the 0−140 m thinness of the Longmaxi formation in this region limits the reserves of shale gas. Due to uplift during the Hercynian orogeny, the Devonian and Carboniferous strata are absent.[26,28] The Permian contains the lower Permian Maokou formation and the upper Permian Longtan formation. The Maokou formation is characterized by limestone with a thickness of 204−459 m, while the Longtan formation consists of limestone and shale with a thickness of 188−242 m.[26]

3. SAMPLES AND METHODS

3.1. Sample Preparations. Shale samples from the marine sedimentary Jiulaodong formation were sourced from a depth of 2749−2751 m the W201 well—a well with industrial-scale gas flow that was drilled by China National Petroleum Corporation (CNPC) in 2011. Cylindrical samples (4 mm diameter) both perpendicular and parallel to the beddings were recovered from core plugs and prepared for FE-SEM, FIB-SEM, and NMR-C experiments (Figure 3).

3.2. Experimental Facilities. *3.2.1. FE-SEM and FIB-SEM.* An FE-SEM equipped with an EDS and FIB-SEM were used to characterize the nanopore structure of the shale samples. The FE-SEM samples were prepared using a 4 mm diameter core drill and argon ion polishing (Figure 3A and B). Both bedding-parallel and -perpendicular surfaces of the shale samples were imaged with a Zeiss Merlin scanning microscope at 5 kV. A voltage of 15 kV was subsequently used to qualitatively analyze minerals and organic matter via EDS (BRUKER XFlash 6130).

The shale samples were placed into the chamber of a ZEISS Crossbeam 540 FIB-SEM and electron-beam-scanned at a vacuum of $<5 \times 10^{-6}$ mbar. The region containing varied organic matter and quartz, calcite, and pyrite was selected as the principal region of interest (ROI). To align the shale sample surface perpendicular to the gallium ion beam, the sample desk was rotated 52° (Figure 4A). Moreover, the ROI was sprayed with a thin layer of Pt to counter any damage from the gallium ion beam. After deposition of Pt, the FIB-SEM automatically milled and imaged the sample layer-by-layer (Figure 4B). The layer thickness was 10 nm, and the selected ROIs

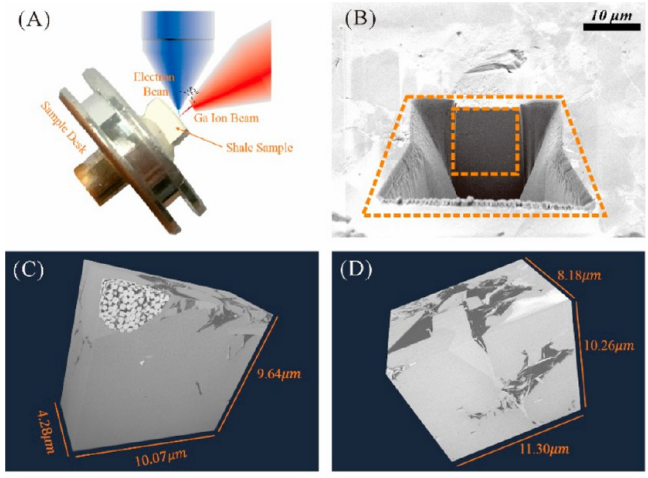

Figure 4. (A) Schematic diagram of the milling and imaging procedure in a FIB-SEM system. (B) Site on the shale sample milled in cross section by the gallium ion beam. (C and D) Two ROIs containing organic matter, quartz, calcite and pyrite, with extents of 10.07 × 9.64 × 4.28 μm^3 and 11.30 × 10.26 × 8.18 μm^3, respectively; voxel size is 10 nm^3.

were 10.07 × 9.64 × 4.28 μm^3 and 11.30 × 10.26 × 8.18 μm^3 respectively (Figure 4C). Avizo 9.0 software was used for analysis of the 2D and 3D micrograph data.

3.2.2. Nuclear Magnetic Resonance Cryoporometry and Nitrogen Adsorption Method Measurement. The NMR-C method is based on the differences in nuclear magnetic resonance relaxation between the freezing or melting point of the fluids in the porous media. Since NMR distinguishes between the solid and liquid states of the permeant (quantifying only the liquid mass) the NMR-C signal gives a clear transition of permeant state with a high signal-to-noise ratio. NMR-C relies on the pore-size-dependent depression of the melting temperature of a pore-filling material given by the Gibbs−Thomson equation,

$$\Delta T_m(x) = T_m^{\infty} - T_m(x) = \frac{4\sigma_{sl} T_m^{\infty}}{x \Delta H_f \rho_s} \quad (1)$$

Here, T_m^{∞} and $T_m(x)$ are the bulk and the pore melting temperatures, σ_{sl} is the solid−liquid surface free energy, ΔH_f is the latent heat of melting, ρ_s is the density of the solid, and x is the pore diameter. For arbitrarily shaped pores, $T_m(x)$ depends on the average curvature of the pore wall rather than on a uniform size parameter such as x. Then eq 1 may be rewritten as

$$\Delta T_m = \frac{K_{GT}}{x} \quad (2)$$

DOI: 10.1021/acs.energyfuels.7b02391
Energy Fuels 2017, 31, 13317−13328

Here, K_{GT} is the melting point depression constant. In a typical experimental protocol, the NMR signal intensity $I(T)$ from the molten fraction of the pore-filling material is measured as the initially frozen sample is incrementally warmed. To separate this signal from that of the frozen fraction, the difference between the transverse relaxation times T_2 in the respective states is exploited. The PSD is then calculated by numerical differentiation of $I(T)$. The PSD can be estimated if the NMR signal intensity is properly calibrated in terms of the mass of the sample. Smaller temperature increments may resolve smaller differential pore sizes and finer PSD features.[11]

In these measurements, the NMR-C shale samples were first pretreated in a drying oven for 24 h at 378.15 K. The dry 4 mm diameter cylindrical shale samples were then placed in 10 mm diameter thin-walled high-resolution NMR sample tubes. The tubes are approximately 2 cm in length and filled with ultrapure water (Figure 3C). The shale samples in the tubes were immersed in water for ~10 h and then centrifuged at 5000 rpm for 3 h at room temperature to help saturate the shales. The NMR-C measurements were conducted in a low field nuclear magnetic resonance device manufactured by Niumag Corporation Ltd., China with a resonance frequency of 21 MHz and a 10 mm probe. The temperature control system consisted of a compressor and a cooling bath to provide a minimum temperature limit of 208.15 K. During the experiments, the temperature was incremented at 0.1−2 K in each step with NMR signal measurements made over 10 min to allow for thermal equilibration at every temperature point.

Shale samples were also characterized by the nitrogen adsorption method (NAM), and the results were then compared to the NMR-C measurements to support the PSDs interpretation. NAM measurements were conducted on a 3H-2000PS2 Instrument at 77.4 K with pulverized shale samples.

3.3. Modeling Methods. *3.3.1. Pore Structure Modeling.* Pore structure modeling is a direct approach to acquire the geometry of the pore space and was employed here to characterize porosity and tortuosity.[31] The first step is to segment the voids. This is achieved simply by using the thresholds from the gray scale image histograms from each slice followed by restacking the binarized three-dimensional images. Based on pore structure modeling, the equivalent pore diameter can also be recovered and is widely used in quantitative analysis defining the PSDs. The equivalent pore diameter can be given as

$$D_{eq} = \sqrt[3]{\frac{6V_{pore}}{\pi}} \tag{3}$$

Here, D_{eq} is the equivalent pore diameter and V_{pore} is the summation of voxels of connected pores. Obviously, eq 3 describes a ball based equivalent pore diameter. However, one difficulty is in accurately separating the connected pores at the correct throat links. Commonly, the connected pores would not be divided in the pore structure modeling especially in the nanopore structure of shales. And then voxels of two or more connected pores are treated as one whole pore in calculating the equivalent pore diameter with eq 3. This exaggerates the pore diameter. Therefore, pore structure modeling is not a good option to quantitatively analyze the PSD in this study.

3.3.2. Pore Network Modeling (PNM). An alternative technique to calculate equivalent pore diameters is to use pore network modeling (PNM). This extracts a topologically representative network with idealized geometric properties derived from the binarized three-dimensional images. We use the PNM method of Dong and Blunt (2009),[32] based on the maximal ball approach[33] where spheres centered on each void voxel are expanded to fill the pore. Both inflating and deflating search algorithms[32] are used to guarantee that the maximal ball is inscribed to the grain or image boundary. In principle, the larger spheres represent pores defined as the larger voids in the rock, whereas the chains of smaller spheres, connected by narrower pathways, define throats. Consequently, the PNM can distinguish pores and throats as well as separate connected pores. Thus, the pore diameter recovered from the PNM is not overestimated, as it may be in pore structure modeling. The pore radius, throat radius, and pore throat length are measured as shown in Figure 5 using Euclidean distances. Moreover, the PNM provides other effective properties of pores and throats such as volume, shape factor, and coordination numbers of pores. Further important output parameters contribute to the analysis of nanopore structure in shales.

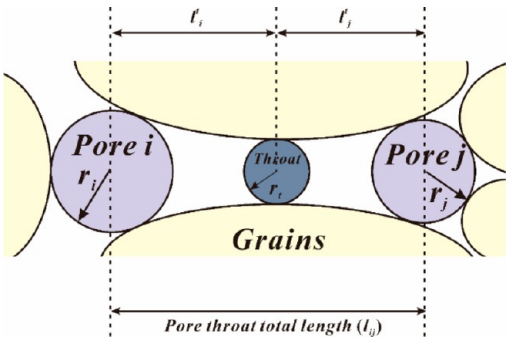

Figure 5. Illustration of the definitions of length and radius for pores and throats of PNM. r_i and r_j are the pore radii, while r_t is the radius of the connective throat. Terms l_i and l_j are the Euclidean distance from pore center to throat center for ***Pore i*** and ***Pore j***, respectively. Term l_{ij} is the pore throat total length, i.e., the Euclidean distance from ***Pore i*** center to ***Pore j*** center (modified after Dong and Blunt, 2009;[32] Hemes et al., 2015[37]).

In this study, 2D micrographs were imaged by FE-SEM for the analysis of nanopore structure in shales. 3D micrographs obtained from FIB-SEM were subsequently segmented into binary images. The segmentation of OM pores in the 3D micrographs were based on an Otsu thresholding algorithm,[34] while IntraP and InterP pores were segmented by an edge detection algorithm in Avizo (due to depth of field issues with the larger size pores resolved by FIB-SEM[35,36]). Both pore structure modeling and PNM were established for OM pores and IntraP/InterP pores in different parts of shales.

4. RESULTS AND DISCUSSIONS

4.1. 2D Pore Structure Analysis. FE-SEM images show that the main voids in the W201 shale samples may be classified into types of meso- and/or microfractures, InterP pores, IntraP pores, and OM pores (Figures 6 and 7). This finding is consistent with previous work.[1,2,14] The voids described here are irregular in shape and extend deep into the matrix. In particular, the image intensity of the OM pores is clearly smaller than that of organic matter; thus, they are easily differentiated from solid in the images. As shown in Figure 6A and B, meso- and/or microfractures are distinct at low magnifications. They commonly occur at micrometer scale or larger, and their initiation and alignment may be related to the mineral grain structure.[38] Viewed on bedding-perpendicular surfaces, the main alignment of meso- and/or microfractures is parallel to the bedding direction as apparent in the texture of the mineral particles. In addition, some of the meso- and/or microfractures are filled with organic matter (Figure 7A and B). The InterP pores exhibit a sheet-like and elongated structure as shown in Figure 7C and E, and the locus of the InterP pores develops around or between clay flakes and brittle mineral grains. The size of the InterP pores commonly ranges from a few micrometers to hundreds of nanometers. IntraP pores observed by FE-SEM occur in grains of various minerals e.g., calcite, and quartz. They are dispersed within the shale matrix (Figure 6B and D), Figure 7B and F). Most of the IntraP pores are a few hundreds of nanometers in diameter and appear isolated in 2D micrographs. The ellipsoidal OM pores are

DOI: 10.1021/acs.energyfuels.7b02391
Energy Fuels 2017, 31, 13317−13328

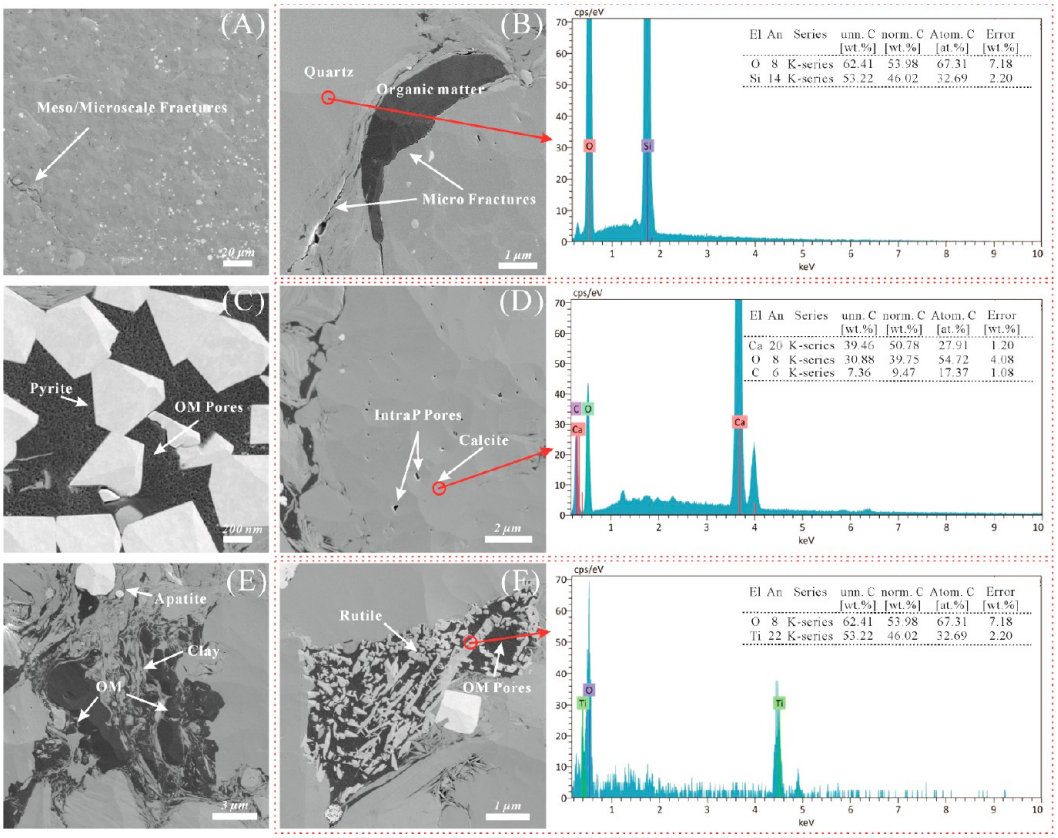

Figure 6. Bedding-perpendicular directional FE-SEM micrographs of the pores and minerals from EDS analysis in the W201 shale samples. (A) Meso- and/or microfractures. (B) Micro fractures, quartz, and organic matter (OM); the spectra from EDS show that the main elements in the selected spot are Si and O, which indicates the mineral is quartz. (C) OM pores in pyrite framboids. (D) IntraP pores in calcite; the spectra from EDS show that the main elements in the selected spot are Ca, O, and C, which indicates the mineral is calcite. (E) Organic matter, clay, and apatite. (F) OM pores in rutile spicules; the spectra from EDS show that the main elements in the selected spot are Ti and O, which indicates the mineral is rutile.

abundant in the organic matter and have a diameter approaching tens of nanometers or as large as a few hundred nanometers (Figure 6C and F, Figure 7D and E).

4.2. Distribution of OM Pores in 2D Images. Previous studies suggest that OM pores are generated during burial and maturation of organic material.[38,39] In these samples, OM pores are found mostly within organic matter that overlaps both clay flakes and pyrite framboids with some also located in rutile spicules (Figure 6C and F, Figure 7D). Few pores are observed in the organic matter occurring between mineral grains of calcite and quartz (Figure 6B and Figure 7B). This indicates that a reducing environment is better for the retention and inversion of organic material as well as for hydrocarbon generation.

In contrast, kerogen may transform into carbon and reduce pores density at a high thermal maturity. This is generally found in the lower Paleozoic shale of southwestern China.[26,29] Moreover, meso- and/or microfractures may be interconnected to form permeability pathways, with those voids beneficial to the storage of free gas. Nanoscale OM pores are potential sites for the storage of adsorbed gas, whereas IntraP pores are mostly isolated in the 2D micrographs. However, FE-SEM micrographs present only the 2D porous microfabric and censor the true 3D pore structure and PSD analysis.

4.3. 3D Pore Structure Analysis. The 3D pore structure is recovered from the layer-by-layer stacked FIB-SEM micrographs. The two ROIs contain OM pores in clay flakes, OM pores in pyrite framboids, and InterP and/or IntraP pores; these were selected by FIB milling (Figure 4C and D).

As shown in Figures 8−13, the sub-ROIs contain more detailed pore information and are extracted from the ROIs results. Six sub-ROIs are selected that contain OM pores in clay flakes, OM pores in pyrite framboids, and InterP/IntraP pores (ordered as OMpores01, OMpores02, OMpores03, PyriteOM-pores, InterP/IntraP01, and InterP/IntraP01 in sequence). The FIB-SEM micrographs, porous segmentation, volume rendering reconstruction, 3D pore structure modeling, and PNM of each sub-ROI in the W021 shale samples are shown in Figures 8−11.

4.3.1. Characteristics of OM Pores in Clay Flakes. The sub-ROI of OMpores01 is 1900 × 2600 × 2200 nm^3, that of OMpores02 is 2580 × 2380 × 1850 nm^3, while that of OMpores02 is 2060 × 410 × 1860 nm^3 (because the organic matter is very thin in this region). These three different regions within the clustered OM pores are from the two ROIs and are randomly chosen. By restacking the FIB-SEM micrographs, the volume rendering reconstructions of the sub-ROIs are directly shown in Figures 8−10B. The bright regions are clay flakes, and the dark regions are organic matter and OM pores. As shown in Figures 8−10A, the OM pores of the sub-ROIs in 3D are segmented into blue by an Otsu thresholding algorithm.[34] The results are applied with an appropriate threshold with the 3D pore structure extracted from modeling of the OM pores and clay flake structures. The OM pore space is in aquamarine as shown in Figures 8−10C. Furthermore, the PNM of the OM

DOI: 10.1021/acs.energyfuels.7b02391
Energy Fuels 2017, 31, 13317−13328

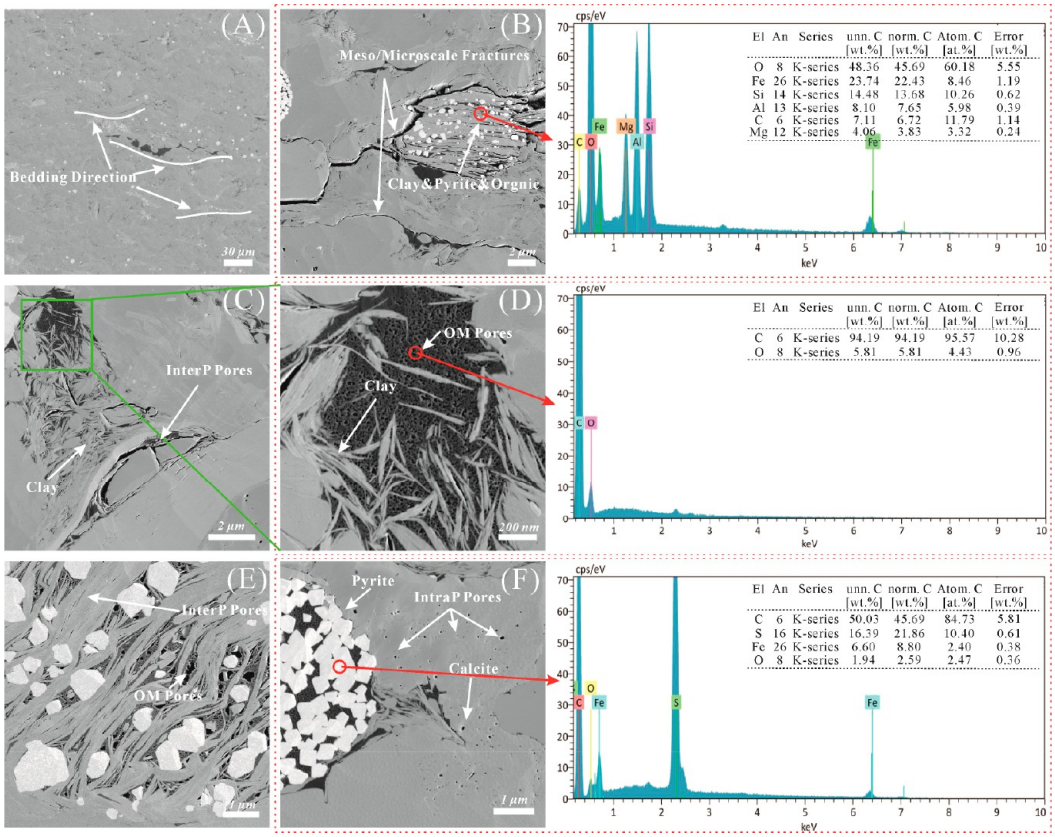

Figure 7. Bedding-parallel directional FE-SEM micrographs of the pore types and minerals from EDS analysis in the W201 shale samples. (A) Bedding direction of minerals and organic matter. (B) Meso- or/and microfractures related to mineral grains structure; the spectra from EDS show that the main elements in the selected spot are basically in line with the composition of clay. (C) InterP pores and overlapping clay flakes. (D) The local enlarged micrograph shown OM pores in clay flakes; the spectra from EDS show that the main elements in the selected spot are C and little O, which indicates the mineral is OM. (E) Organic matter and pores in overlapping clay flakes. (F) OM pores in pyrite framboids and intrapores in calcite; the spectra from EDS show that the main elements in the selected spot are C, Fe, S, and little O, which indicates the point of EDS covers both pyrite and OM.

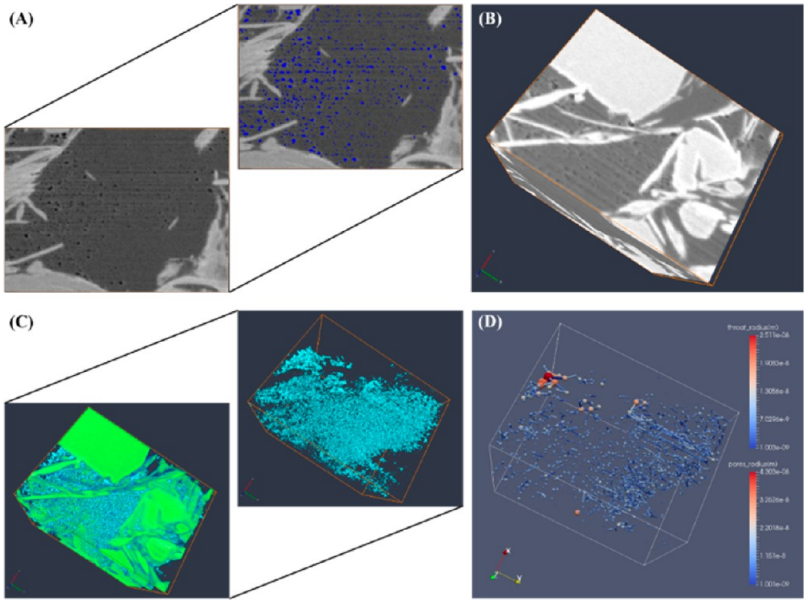

Figure 8. Results of the pore structure of OMpores01. (A) OM pore segmentation with an Otsu thresholding algorithm. (B) Volume rendering reconstruction of sub-ROIs of OMpores01 (1900 × 2600 × 2200 nm^3): the bright regions are clay flakes, and the dark regions are organic matter and OM pores. (C) Pore structure modeling with OM pores in aquamarine and clay flakes in green. (D) The PNM of OMpores01.

DOI: 10.1021/acs.energyfuels.7b02391
Energy Fuels 2017, 31, 13317−13328

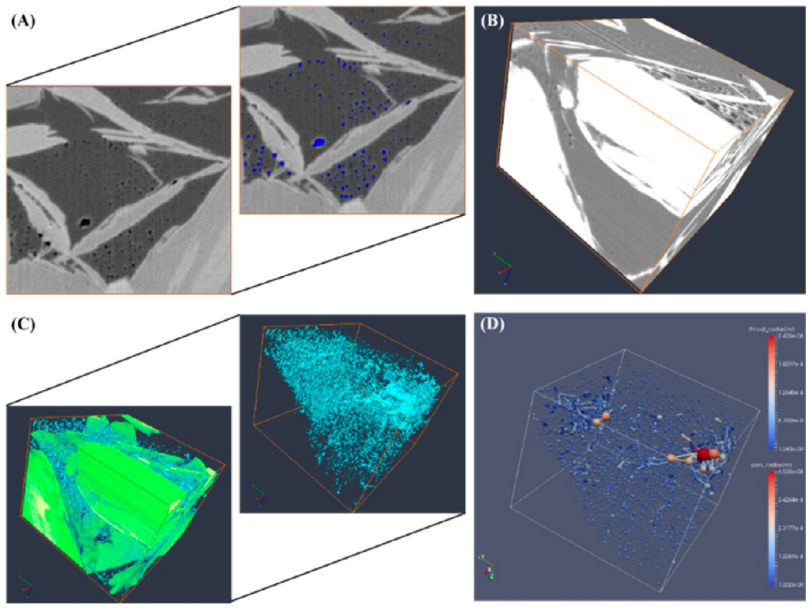

Figure 9. Results of the pore structure of OMpores02. (A) OM pore segmentation with an Otsu thresholding algorithm. (B) Volume rendering reconstruction of sub-ROIs of OMpores02 (2580 × 2380 × 1850 nm^3) with bright regions depicting clay flakes and the dark regions depicting organic matter and OM pores. (C) Pore structure modeling: OM pores are in aquamarine, and clay flakes are in green. (D) The PNM of OMpores02.

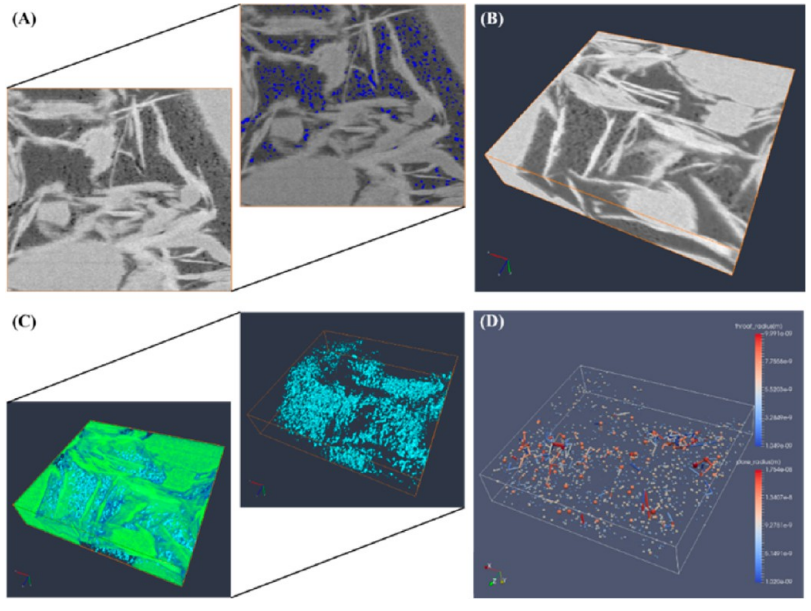

Figure 10. Results of the pore structure of OMpores03. (A) OM pore segmentation with an Otsu thresholding algorithm. (B) Volume rendering reconstruction of sub-ROIs of OMpores03 (2060 × 410 × 1860 nm^3) with bright regions depicting clay flakes and the dark regions depicting organic matter and OM pores. (C) Pore structure modeling: OM pores are in aquamarine and clay flakes are in green. (D) The PNM of OMpores03.

pores obtained from the modeling[32] is also shown with a cool (small pores) to warm (large) color scale in Figures 8−10D. Combined with the results above, the OM pores in the W201 shale samples exhibit good interconnectivity. However, due to the presence of clay flakes, the connected OM pores are fragmented, and the isolated pores are also widely distributed in the organic matter. In addition, the connection between the OM pores and the exterior is blocked. The information on the OM pores recovered from FIB-SEM is significantly more detailed than that from 2D FE-SEM.

4.3.2. Characteristics of OM Pores in Pyrite Framboids. The sub-ROIs of PyriteOMpores is 2000 × 1500 × 950 nm^3 and are shown in Figure 11 with a volume rendering reconstruction exhibited in Figure 11B. The bright regions are pyrite framboids, and the dark regions are organic matter and OM pores. The exterior gray regions are minerals (Figure 11A). From the gray histogram the OM pores were segmented into blue with an appropriate threshold in Figure 11A. The 3D pore structure modeling of the OM pores and pyrite framboids are shown in Figure 11C. The OM pores are in aquamarine, while the polyhedral pyrite crystals are in orange. The PNM is also exhibited in Figure 11D, and the density of throats in PyriteOMpores is clearly less than that for the OM pores above.

DOI: 10.1021/acs.energyfuels.7b02391
Energy Fuels 2017, 31, 13317−13328

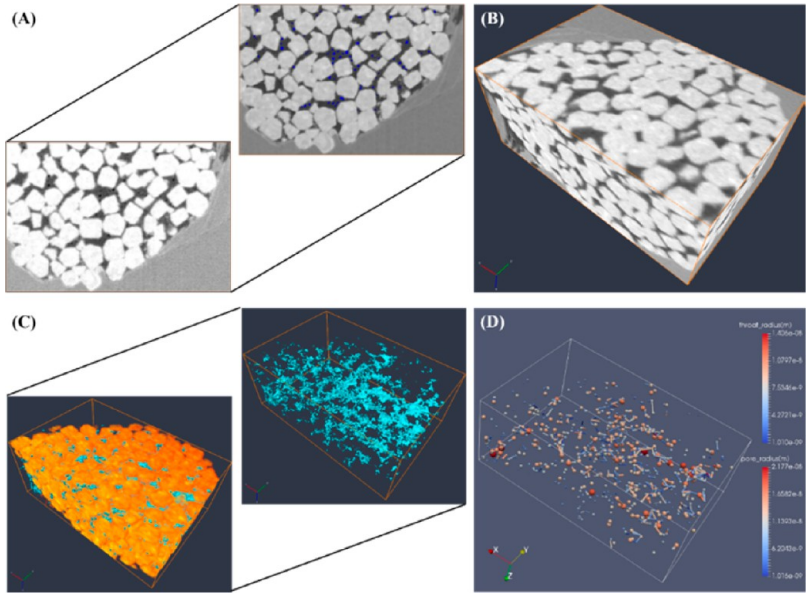

Figure 11. Results for the pore structure of PyriteOMpores. (A) OM pore segmentation with an Otsu thresholding algorithm. (B) Volume rendering reconstruction of sub-ROIs of PyriteOMpores (2000 × 1500 × 950 nm^3) with bright regions showing pyrite framboids and dark regions showing organic matter and OM pores. (C) Pore structure modeling with OM pores as aquamarine and pyrite framboids as orange. (D) The PNM of PyriteOMpores.

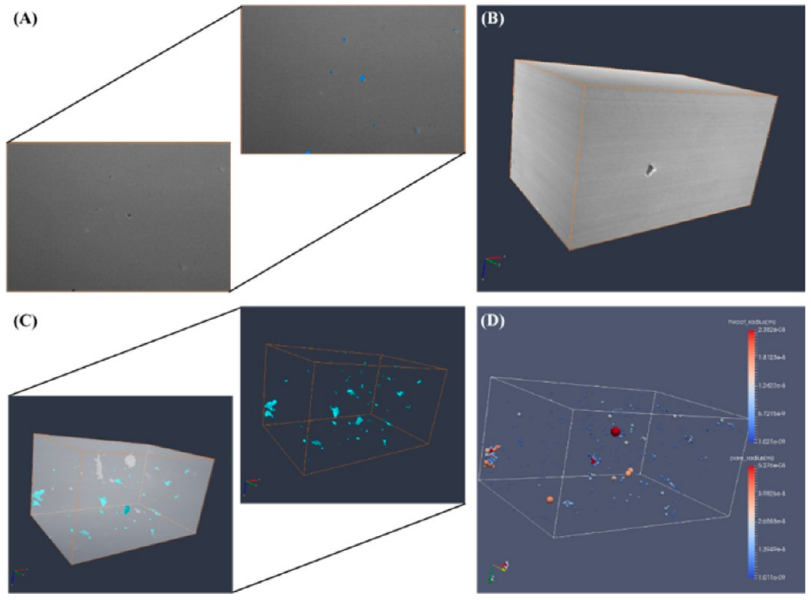

Figure 12. Pore structure of InterP/IntraP01. (A) InterP and IntraP pores segmented with an edge detection algorithm. (B) Volume rendering reconstruction of sub-ROIs of InterP/IntraP01 (6500 × 4300 × 3610 nm^3). (C) Pore structure modeling: InterP and IntraP pores are in aquamarine and pyrite in bright gray. (D) The PNM of InterP/IntraP01.

4.3.3. Characteristics of InterP and IntraP Pores. Both InterP and IntraP pores were difficult to distinguish in the grayscale FIB-SEM micrographs. Therefore, the sub-ROIs were ordered as InterP/IntraP01 and InterP/IntraP02, which combined these two types of pores together (6500 × 4300 × 3610 nm^3 and 2060 × 4350 × 3790 nm^3 in size) and extracted from the two ROIs, respectively (Figures 12 and 13). The volume rendering reconstructions of InterP/IntraP01 and InterP/IntraP02 are shown in Figures 12−13B. Thresholding segmentation could not successfully extract pores from the grayscale micrographs because of the depth of field phenomenon for the bigger pores in FIB-SEM (the high gray level around the pore edges appears irregular and in different shades within the pore). Alternatively, an edge detection algorithm in Avizo is used to segment the InterP and IntraP pores. The blue areas in Figures 12−13A are the segmentation results of the pores. Figures 12−13C show the 3D pore structure modeling of the InterP/IntraP01 and InterP/IntraP02 as established by Avizo. The bright gray regions are pyrite, and aquamarine regions are void space. Furthermore, the PNM of InterP/IntraP01 and InterP/IntraP02 are shown in Figure 12−13D indicating that isolated pores are dominant in these sub-ROIs. This suggests that the connectivity could be poor. However, the connectivity of the InterP pores in the 2D FE-

DOI: 10.1021/acs.energyfuels.7b02391
Energy Fuels 2017, 31, 13317−13328

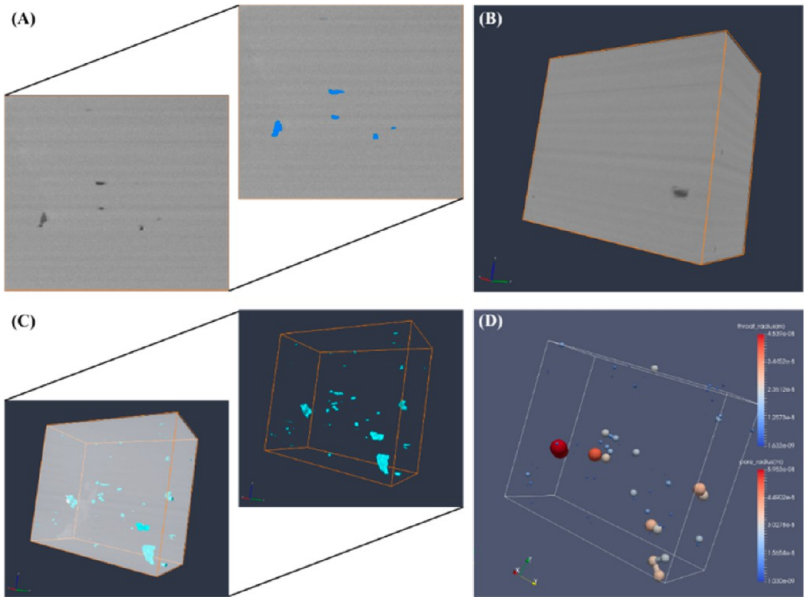

Figure 13. Pore structure of InterP/IntraP02. (A) InterP and IntraP pores segmented with an edge detection algorithm. (B) Volume rendering reconstruction of sub-ROIs of InterP/IntraP02 (2060 × 4350 × 3790 nm^3). (C) Pore structure modeling: InterP and IntraP pores are in aquamarine. (D) The PNM of InterP/IntraP02.

Table 1. Characteristic Parameters of Pore Structure in Shale Samples from the W201 Well As Recovered from Pore Structure Modeling and PNM

Sub-ROIs	Size (voxel/10 nm^3)	Porosity (%)	Average pore diameter (nm)	Total no. of pores	Average throat length (nm)	Total no. of throats	Tortuosity
OMpores01	190 × 260 × 220	2.82	14.23	33 638	18.8	1683	3.81
OMpores02	258 × 238 × 185	2.01	14.24	22 967	20.2	657	4.33
OMpores03	206 × 41 × 186	3.13	14.22	3718	19.3	364	5.57
PyriteOMpores	200 × 150 × 95	1.88	20.41	968	22.5	549	7.21
InterP/IntraP01	650 × 430 × 361	0.136	92.46	226	24.9	231	—
InterP/IntraP02	206 × 435 × 379	0.115	105.75	88	33.8	17	—

SEM micrographs seems well developed along the mineral orientation. Consequently, the connectivity of the pores could be observed not only by FE-SEM but also by FIB-SEM as well.

4.4. Characteristic Parameters of 3D Pore Structure. The characteristic parameters of the various types of pore structure in shale samples recoverd from the W201 well are listed in Table 1. They are recovered from pore structure modeling and PNM. The porosity is approximately 2.82%, 2.01%, and 3.13% for OMpores01, OMpores02, and OMpores03, respectively. The value is 1.88% for PyriteOMpores and 0.136% and 0.115% for InterP/IntraP01 and InterP/IntraP02, respectively. This indicates that the porosity of the OM pores (including OM pores in pyrite framboids) is much higher than that in InterP and IntraP pores. This implies that OM pores are the dominant pore type in shale samples and provide significant space for the storage of gas. However, the average pore diameter of the OM pores is much smaller than that of the InterP and IntraP pores. Consequently, the individual volume of InterP and IntraP pores is almost 3 orders of magnitude higher than that of OM pores.

In terms of quantity, the preponderance of OM pores is in clay flakes (Table 1). OM pores in pyrite framboids are obviously lower because polymorph crystals chiefly occupy the available pore space. This may also be the reason that tortuosity (the ratio between the length of the path and the distance between its ends along the specified axis) of the OM pores in pyrite framboids is higher than that of OM pores in clay flakes (Table 1). Moreover, InterP and IntraP pores are rare and have very high (indeterminate) tortuosity due to their isolation.

4.5. PSD Comparison from PNM and NMR-C. Figure 14 shows the NMR-C spectra distribution of the bulk cylindrical shale sample, the PSD from NAM of the pulverized shale sample, and the PSD of the six sub-ROIs from different locations of this bulk sample using PNM. The transverse relaxation time (T2) of NMR-C can be translated into an equivalent pore size, and NMR T2 spectra distributions can also reflect the corresponding PSD.[9,12,24] The peaks of PSD from NMR-C and NAM are well matched in Figure 14A, which shows the NMR-C method has good credibility compared with the common method. However, the total porosity from NAM seems larger than that from NMR-C. This is because pulverized shale samples were used in NAM measurement. Some isolated pores were connected during the pulverizing process so the porosity was increased,[24] as well as the adsorption volume. As shown in Figure 14A, the PSD from the NMR-C has multiple discontinuous peaks ranging from 1.86 to 142.86 nm. This reflects that at least four distinct scales of pore sizes are present in the W201 shale samples. In Figure 14B, the bimodal PSD of OMpores01 recovered from the PNM matches well with the PSD recovered from NMR-C at least for peaks in the ranges 5−8 nm and 10−20 nm. And the left peak of the PSD of OMpores01 from the PNM is significantly lower than the right one. Contrastingly, the left peak of the PSD from NMR-C in 5−8 nm is higher than the right one in 10−20 nm. Moreover,

DOI: 10.1021/acs.energyfuels.7b02391
Energy Fuels 2017, 31, 13317−13328

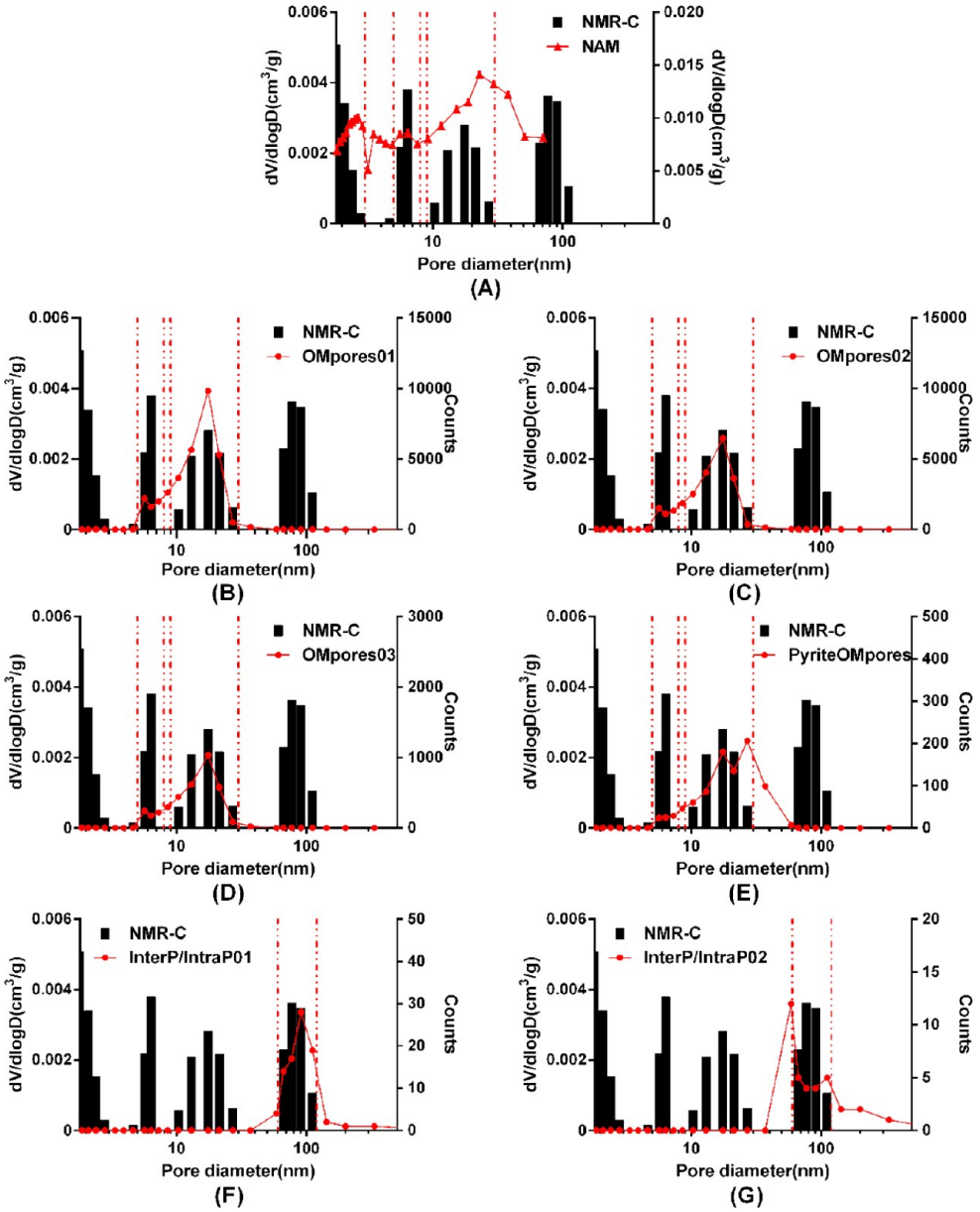

Figure 14. (A) Histogram of PSDs from NMR-C, left Y axis, with polylines depicting the PSDs from the NAM, right Y axis. (B–G) Histogram of PSDs from NMR-C, left Y axis, with polylines depicting the PSDs of pores in each sub-ROI from (in different locations) PNM, right Y axis.

the same situation goes for PSDs of OMpores02 and OMpores03 from the PNM in Figure 14C and D. This result indicates that the peaks of the PSD from NMR-C are 5–8 nm and 10–20 nm, which correspond to the peaks of the OM pores in clay flakes. On the other hand, the lower left peak of PSD from PNM may be because of the spatial resolution. This limits the pore extraction of PNM. The two left discontinuous peaks of PSD from NMR-C in the ranges from 1.86–3 nm and 5–8 nm are much higher, and this is because NMR-C has higher sensitivity and accuracy in detecting nanopores.

As shown in Figure 14E, the PSD of PyriteOMpores has wider pore distribution, which implies that a reducing environment is better for development of porosity. It also consists of bigger average pore diameters in Table 1. Furthermore, The PSDs of InterP/IntraP01 and InterP/IntraP02 almost exactly match the right-most peak of PSD from NMR-C, which ranges from 60 to 120 nm (Figure 14F and G). This result shows that the right-most peak of PSD from NMR-C is the amplitude of NMR signal excited by InterP and IntraP pores. These pores have an obvious distinction compared to OM pores in size whether it is in PNM or NMR-C. And some studies also suggest that pores in inorganic mineral crystal, i.e. quartz, calcite, play important roles in transport behavior of gas or oil in shale.[40,41] Furthermore, the results indirectly demonstrate that water molecules entered into nanoscale OM pores and InterP and IntraP pores through the shale during the centrifugal saturated preprocess of NMR-C.

5. CONCLUSION

The 2D/3D nanopore structure of shale samples from the W201 well were quantitatively measured by FE-SEM, FIB-SEM, and NMR-C. The 2D FE-SEM micrographs suggests that OM pores as well as hydrocarbon generation mostly develop within organic matter within a reducing environment. This environment is confirmed by the proximity of clay flakes, pyrite framboids, and rutile spicules. Nanoscale OM pores have the

DOI: 10.1021/acs.energyfuels.7b02391
Energy Fuels 2017, 31, 13317–13328

potential for storage of adsorbed gas. IntraP pores are mostly isolated in the 2D micrographs. Moreover, meso- and/or microfractures may be interconnected to form permeability pathways and are beneficial to the storage of free gas and to gas transport.

A 3D pore structure model and PNM are established for both OM pores and InterP and IntraP pores. The interconnectivity of the OM pores adjacent to clay flakes is higher than that in pyrite framboids because pyrite crystals largely occupy the space. Conversely, InterP and IntraP pores are mostly isolated in sub-ROIs, with poor connectivity. The porosity of the OM pores (including OM pores in pyrite framboids) is much higher than that of the InterP and IntraP pores. This implies that the OM pores are the dominant pore type and offer the principal space for gas storage in the shale matrix. The individual volume of the InterP and IntraP pores is almost 3 orders of magnitude higher than that of the OM pores since the average pore diameter of the OM pores is much smaller than that of the InterP and IntraP pores.

The PSD results indicate that the peaks of the PSD from NMR-C are in the ranges 5−8 nm and 10−20 nm and correspond to the peaks of the OM pores from PNM. This suggests that the NMR-C signal in this range is sensitive to the OM pores. In addition, NMR-C has higher sensitivity and accuracy in detecting nanopores. Furthermore, The PSDs of InterP and IntraP pores range from 60 to 120 nm. This matches almost exactly with the right-most peak of the PSD recovered from NMR-C, illustrating that the NMR-C signals in this range are excited by the InterP and IntraP pores. The results indirectly demonstrate that water is indeed able to enter into nanoscale OM pores and InterP and IntraP pores during the centrifugal saturation preprocess of NMR-C.

The nanopore structural characteristics in shale samples are vital for shale gas development. This study explores the correspondence of PSDs of shales between PNMs and NMR-C and demonstrates that combining FIB-SEM and NMR-C can be a promising technique in detecting and characterizing the nanoporosity of shales.

AUTHOR INFORMATION

Corresponding Author

*E-mail: dongyh@mail.iggcas.ac.cn.

ORCID

Yanhui Dong: 0000-0003-4815-8600

Notes

The authors declare no competing financial interest.

ACKNOWLEDGMENTS

This work was financially supported by Strategic Priority Research Program of the Chinese Academy of Sciences (Grant No. XDB10030601) and Youth Innovation Promotion Association, CAS (Grant No. 2016063). The authors specially thank working staffs at Multi-Scale Imaging and Characterization Laboratory, IGGCAS in Beijing and Minyue Zhou for their aid in both conducting the experiments and analyzing the data.

NOMENCLATURE

FIB-SEM = Focused Ion Beam Scanning Electron Microscopy
NMR = Nuclear Magnetic Resonance
NMR-C = Nuclear Magnetic Resonance Cryoporometry
EDS = X-ray Energy Dispersive Spectroscopy
FE-SEM = Field-Emission Scanning Electron Microscopy
Nano-XCT = Nano X-ray computed tomography
InterP pores = interparticle pores
IntraP pores = intraparticle pores
OM pores = pores in organic matter
PNM = pore-network modeling
PSD = pore size distribution
NAM = the nitrogen adsorption method

REFERENCES

(1) Clarkson, C. R.; Solano, N.; Bustin, R. M.; et al. Pore structure characterization of North American shale gas reservoirs using USANS/SANS, gas adsorption, and mercury intrusion. *Fuel* **2013**, *103* (1), 606−616.

(2) Wang, Y.; Pu, J.; Wang, L.; et al. Characterization of typical 3D pore networks of Jiulaodong formation shale using nano-transmission X-ray microscopy. *Fuel* **2016**, *170*, 84−91.

(3) Chen, L.; Zhang, L.; Kang, Q.; et al. Nanoscale simulation of shale transport properties using the lattice Boltzmann method: permeability and diffusivity. *Sci. Rep.* **2015**, *5*, 8089.

(4) Luo, Q.; Zhong, N.; Dai, N.; et al. Graptolite-derived organic matter in the Wufeng−Longmaxi Formations (Upper Ordovician−Lower Silurian) of southeastern Chongqing, China: Implications for gas shale evaluation. *Int. J. Coal Geol.* **2016**, *153* (1−2), 87−98.

(5) Wang, P.; Jiang, Z.; Chen, L.; et al. Pore structure characterization for the Longmaxi and Niutitang shales in the Upper Yangtze Platform, South China: Evidence from focused ion beam−He ion microscopy, nano-computerized tomography and gas adsorption analysis. *Mar. Pet. Geol.* **2016**, *77*, 1323−1337.

(6) Wang, S. F.; Dong, D. Z.; Wang, Y. M.; et al. A comparative study of the geological feature of marine shale gas between China and the united states. *Natural Gas Geoscience* **2015**, *26* (9), 1666−1678.

(7) Fishman, N. S.; Hackley, P. C.; Lowers, H. A.; et al. The nature of porosity in organic-rich mudstones of the Upper Jurassic Kimmeridge Clay Formation, North Sea, offshore United Kingdom. *Int. J. Coal Geol.* **2012**, *103* (23), 32−50.

(8) Lee, S.; Fischer, T. B.; Stokes, M. R.; et al. Dehydration Effect on the Pore Size, Porosity, and Fractal Parameters of Shale Rocks: Ultrasmall-Angle X-ray Scattering Study. *Energy Fuels* **2014**, *28* (11), 6772−6779.

(9) Li, J.; Zhou, S.; Fu, D.; et al. Changes in the pore characteristics of shale during comminution. *Energy Explor. Exploit.* **2016**, *34* (5), 676−688.

(10) Curtis, M. E.; Ambrose, R. J.; Sondergeld, C. H. Structural characterization of gas shales on the micro-and nano-scales. Canadian unconventional resources and international petroleum conference. Society of Petroleum Engineers: 2010.

(11) Loucks, R. G.; Reed, R. M.; Ruppel, S. C.; et al. Morphology, Genesis, and Distribution of Nanometer-Scale Pores in Siliceous Mudstones of the Mississippian Barnett Shale. *J. Sediment. Res.* **2009**, *79* (12), 848−861.

(12) Zhang, Q.; Dong, Y.; Liu, S. Shale Pore Characterization Using NMR Cryoporometry with Octamethylcyclotetrasiloxane as the Probe Liquid. *Energy Fuels* **2017**, *31* (7), 6951.

(13) Chen, Y.; Wei, L.; Mastalerz, M.; et al. The effect of analytical particle size on gas adsorption porosimetry of shale. *Int. J. Coal Geol.* **2015**, *138*, 103−112.

(14) Curtis, M. E.; Sondergeld, C. H.; Ambrose, R. J.; et al. Microstructural investigation of gas shales in two and three dimensions using nanometer-scale resolution imaging. *AAPG Bull.* **2012**, *96* (4), 665−677.

(15) Hou, Y.; He, S.; Yi, J.; et al. Effect of pore structure on methane sorption potential of shales. *Petroleum Exploration & Development* **2014**, *41* (2), 272−281.

(16) Ma, Y.; Pan, Z.; Zhong, N.; et al. Experimental study of anisotropic gas permeability and its relationship with fracture structure of Longmaxi Shales, Sichuan Basin, China. *Fuel* **2016**, *180*, 106−115.

DOI: 10.1021/acs.energyfuels.7b02391
Energy Fuels 2017, 31, 13317−13328

(17) Javadpour, F.; Fisher, D.; Unsworth, M. Nanoscale gas flow in shale gas sediments. *Journal of Canadian Petroleum Technology* **2007**, *46*, 10.
(18) Loucks, R. G.; Reed, R. M.; Ruppel, S. C.; et al. Spectrum of pore types and networks in mudrocks and a descriptive classification for matrix-related mudrock pores. *AAPG Bull.* **2012**, *96* (6), 1071−1098.
(19) Wu, S.; Zhu, R.; Cui, J.; et al. Characteristics of lacustrine shale porosity evolution, Triassic Chang 7 Member, Ordos Basin, NW China. *Petroleum Exploration & Development* **2015**, *42* (2), 185−195.
(20) Ma, Y.; Zhong, N. N.; Huang, X. Y.; et al. The application of focused ion beam scanning electron microscope (FIB-SEM) to the nanometer-sized pores in shales. *Journal of Chinese Electron Microscopy Society* **2014**, *33* (3), 251−256.
(21) Sun, H.; Yao, J.; Cao, Y. C.; et al. Characterization of gas transport behaviors in shale gas and tight gas reservoirs by digital rock analysis. *Int. J. Heat Mass Transfer* **2017**, *104*, 227−239.
(22) Firouzi, M.; Rupp, E. C.; Liu, C. W.; et al. Molecular simulation and experimental characterization of the nanoporous structures of coal and gas shale. *Int. J. Coal Geol.* **2014**, *121* (1), 123−128.
(23) Fleury, M.; Fabre, R.; Webber, J. B. W. Comparison of pore size distribution by NMR relaxation and NMR cryoporometry in shales. *SCA*, **2015**.
(24) Zhang, Q.; Dong, Y. H.; Tong, S. Q.; et al. Nuclear magnetic resonance cryoporometry as a tool to measure pore size distribution of shale rock. *Chin. Sci. Bull.* **2016**, *61*, 2387−2394 (in Chinese).
(25) Li, Z.; Qi, Z.; Shen, X. Research on Quantitative Analysis for Nanopore Structure Characteristics of Shale Based on NMR and NMR Cryoporometry. *Energy Fuels* **2017**, *31*, 5844−5853, DOI: 10.1021/acs.energyfuels.7b00170.
(26) Zhou, Q.; Xiao, X.; Tian, H.; et al. Modeling free gas content of the Lower Paleozoic shales in the Weiyuan area of the Sichuan Basin, China. *Mar. Pet. Geol.* **2014**, *56* (3), 87−96.
(27) Wei, G.; Chen, G.; Du, S.; et al. Petroleum systems of the oldest gas field in China: Neoproterozoic gas pools in the Weiyuan gas field, Sichuan Basin. *Mar. Pet. Geol.* **2008**, *25* (4−5), 371−386.
(28) Dai, J. Pool-forming periods and gas sources of Weiyuan gasfield. *Petroleum Geology & Expeximent* **2003**, *25* (5), 473−480.
(29) Borkloe, J. K.; Pan, R.; Jin, J.; et al. Evaluation of shale gas potential of Cambrian Jiulaodong Formation in Wei-201 well block in Sichuan Basin, China. *Interpretation* **2016**, *4* (2), T123−T140.
(30) Li, W.; Yu, H.; Deng, H. Stratigraphic division and correlation and sedimentary characteristics of the Cambrian in central-southern Sichuan Basin. *Petroleum Exploration & Development* **2012**, *39* (6), 725−735.
(31) Blunt, M. J.; Bijeljic, B.; Dong, H.; et al. Pore-scale imaging and modelling. *Adv. Water Resour.* **2013**, *51* (1), 197−216.
(32) Dong, H.; Blunt, M. J. Pore-network extraction from micro-computerized-tomography images. *Phys. Rev. E* **2009**, *80* (3), 036307.
(33) Silin, D.; Patzek, T. Pore space morphology analysis using maximal inscribed spheres. *Phys. A* **2006**, *371* (2), 336−360.
(34) Gharbi, O.; Blunt, M. J. The impact of wettability and connectivity on relative permeability in carbonates: A pore network modeling analysis. *Water Resour. Res.* **2012**, *48* (12), 3945−3952.
(35) Jing, Y.; Wu, X. C.; Wu, Y. C.; et al. Study on extending the depth of field in reconstructed image for a micro digital hologram. *Acta Physica Sinica* **2015**, *64* (11), 114209.
(36) Sun, L.; Wang, X.; Jin, X.; et al. Three dimensional characterization and quantitative connectivity analysis of micro/nano pore space. *Petroleum Exploration & Development Online* **2016**, *43* (3), 537−546.
(37) Hemes, S.; Desbois, G.; Urai, J. L.; et al. Multi-scale characterization of porosity in Boom Clay (HADES-level, Mol, Belgium) using a combination of X-ray μ-CT, 2D BIB-SEM and FIB-SEM tomography. *Microporous Mesoporous Mater.* **2015**, *208*, 1−20.
(38) Slatt, R. M.; O'Brien, N. R. Pore types in the Barnett and Woodford gas shales: Contribution to understanding gas storage and migration pathways in fine-grained rocks. *AAPG Bull.* **2011**, *95* (12), 2017−2030.
(39) Jarvie, D. M.; Hill, R. J.; Ruble, T. E.; et al. Unconventional shale-gas systems: The Mississippian Barnett Shale of north-central Texas as one model for thermogenic shale-gas assessment. *AAPG Bull.* **2007**, *91* (4), 475−499.
(40) Wang, S.; Feng, Q.; Javadpour, F. Breakdown of Fast Mass Transport of Methane through Calcite Nanopores. *J. Phys. Chem. C* **2016**, *120* (26), 14260.
(41) Wang, S.; Javadpour, F.; Feng, Q. Molecular dynamics simulations of oil transport through inorganic nanopores in shale. *Fuel* **2016**, *171*, 74−86.

DOI: 10.1021/acs.energyfuels.7b02391
Energy Fuels 2017, 31, 13317−13328